WARWICK
THE UNIVERSITY OF WARWICK

Manuscript version: Author's Accepted Manuscript
The version presented in WRAP is the author's accepted manuscript and may differ from the published version or Version of Record.

Persistent WRAP URL:
http://wrap.warwick.ac.uk/149142

How to cite:
Please refer to published version for the most recent bibliographic citation information. If a published version is known of, the repository item page linked to above, will contain details on accessing it.

Copyright and reuse:
The Warwick Research Archive Portal (WRAP) makes this work by researchers of the University of Warwick available open access under the following conditions.

Copyright © and all moral rights to the version of the paper presented here belong to the individual author(s) and/or other copyright owners. To the extent reasonable and practicable the material made available in WRAP has been checked for eligibility before being made available.

Copies of full items can be used for personal research or study, educational, or not-for-profit purposes without prior permission or charge. Provided that the authors, title and full bibliographic details are credited, a hyperlink and/or URL is given for the original metadata page and the content is not changed in any way.

Publisher's statement:
Please refer to the repository item page, publisher's statement section, for further information.

For more information, please contact the WRAP Team at: wrap@warwick.ac.uk.

warwick.ac.uk/lib-publications

Tensorial Permeability Microstructure Model Considering Crystallographic Texture and Grain Size for Evaluation of Magnetic Anisotropy In Polycrystalline Steels

Jun Liu*† and Claire Davis

Advanced Steel Research Centre, Warwick Manufacturing Group, University of Warwick, Coventry CV4 7AL, United Kingdom

ARTICLE HISTORY

Compiled February 12, 2021

ABSTRACT

A finite element microstructure model with permeability tensors that considers crystallographic texture and grain size based on magnetic domain theory has been developed for the evaluation of magnetic anisotropy in polycrystalline steels. The model has proved capable of capturing the crystallographic texture, the grain size and the vector induction effects on the effective permeability behaviours for typical textures in steels. The predicted magnetic properties as a function of the magnetic field direction enables a quantitative characterisation of the magnetic anisotropy. The predicted effective permeability maps can serve as a visual indication of the crystallographic texture from magnetic values. These features have been experimentally validated against a commercial grain oriented electrical steel featuring strong texture and magnetic anisotropy.

KEYWORDS

Permeability tensor; Finite Element; Microstructure; Crystallographic texture; Steels

1. Introduction

Iron and steel crystal structures are magnetically anisotropic due to the alignment of magnetic dipoles in a crystal cell [1]. It has also been experimentally confirmed that the cube edges ($\langle 100 \rangle$) and the cube diagonals ($\langle 111 \rangle$) are the easiest and the hardest directions of mag-

*CONTACT Jun Liu. Email: liuj118@cardiff.ac.uk

† Current affiliation: School of Engineering, Cardiff University, Cardiff CF24 3AA, UK

netising respectively in iron [2] and silicon-iron [3] single crystals. This fundamental magnetic anisotropy is inherited by each grain in polycrystalline steels. If grains are randomly orientated, the anisotropy effect averages out and, as a result, the steels exhibit isotropic behaviours. If there are preferred crystallographic orientations present, often referred to as crystallographic texture, the overall average properties have a certain anisotropy associated with the texture. This simple yet useful averaging approach has been applied to predict anisotropic mechanical properties of polycrystalline materials, e.g., elastic modulus, based on the corresponding single-crystal properties, with differences in specific approximations including Reuss [4], Voigt [5], Hill [6] and finite element (FE) [7] models. In a similar manner Daniel et al [8] estimated the scalar effective magnetic permeability of polycrystalline materials based on an empirical single crystal anisotropy and effective medium approximations. L. Kestens [9] took a more basic and simplified approach proposing an 'A' parameter, as opposed to a fundamental magnetic property, that averages the minimum angle between the magnetisation (implicitly assumed to be homogeneous) and the closest easy direction to characterise the so-called magnetic quality of a given texture for non-oriented electrical steels.

Both Daniel's and Kestens' model overlooked some important aspects of the microstructure, in particular, the morphology of individual grains as well as the microstructure as a whole, which can also influence the magnetic flux behaviours and hence the effective permeability. The models work well for uniform equiaxed single phase material but cannot be extended to more complex microstructures. For example, alignment in the microstructure, especially second phase, often occurs during steel processing, e.g., rolling [10], and sometimes is present in the final product, e.g., in superduplex stainless steel (banded austenite and ferrite structures), dual phase steels (banded ferrite and martensite) or hot rolled C-Mn grades (banded ferrite and pearlite structures) and can also give rise to magnetic anisotropy. Zhou et al [11] predicted the effective permeability for dual-phase steel microstructures represented by digitised and processed (recognising different phases) real micrographs by FE modelling. Whilst the approach enables studying the separate effects of aligned microstructures, phase balance, and more recently grain size [12], their model does not consider the effect of crystallographic texture, which may give misleading prediction and interpretation if textures also play a significant role on magnetic properties in the measurement direction and on anisotropy.

There is an important implicit assumption in the scalar permeability models that the magnetic flux density B always parallels with the applied field H, which is only a valid approximation at low and uniform fields. Some tensor permeability models [13–16] have been reported to be

able to address this limitation, which also facilitates finite element modelling [17–19] to solve problems that involve rotational fields and complex geometry. Nevertheless, tensor models require prior knowledge of the permeability for principal directions, along which B parallels with H, to formulate a permeability tensor. Note the principal directions are not readily known or necessarily exist in polycrystalline materials. Some models [13, 14] simply took two orthogonal directions with maximum and minimum permeability as the principal directions and their values as the elements of a diagonal tensor [13]. This basic approach fails when the maximum and the minimum permeability occur in non-orthogonal directions, e.g., in grain oriented electrical steels (GOES). Others went the extra length to formulate a non-diagonal tensor and obtain the principal directions and the corresponding permeability values by finding the eigenvalues and eigenvectors of the tensor [15]. All these empirical permeability tensors can not predict the anisotropy for given crystallographic textures but only deal with rotational fields, which could be experimentally applied by a rotational single sheet tester [20, 21] or be present in electrical steel components in motors, in the presence of known magnetic anisotropy. Some vector hysteresis models based on the Presiach model, e.g., [22], or the Jiles-Atherton model, e.g., [23, 24], have also been reported to model anisotropy hysteresis behaviours associated with rotational fields. Again, none of these hysteresis models can predict the magnetic anisotropy associated with crystallographic textures.

There are no reports of a permeability tensor for a cubic single crystal that can fully describe the observed anisotropy and symmetry. According to the Neumann's principle, the tensor representing any physical property of a crystal should be invariant with regard to the symmetry operation of the crystal class. In the case of cubic crystals such as electrical steel, the permeability tensor that satisfies all the symmetries must reduce to a scalar [25]. It follows that the corresponding magnetic properties should be isotropic, which would be inconsistent with experiments [2, 3]. This paradox rendered the tensorial approach inapplicable as far as the cubic crystallographic texture is concerned and thereby make people resort to empirical approaches using scalar permeability e.g., [8]. The fundamental reason is that the magnetic structure of, say, α–iron does not have all the symmetries of the crystal structure. Magnetic domains exist in ferromagnetic materials; there are more than one direction of magnetic domains even in a single crystal. Their magnetic structure has a lower symmetry than the crystal structure itself does as illustrated in Fig. 1 due to the directionality of the magnetic spin. In this paper, we propose a solution to this paradox by formulating the fundamental permeability tensor at the magnetic domain level without violating the general Neumann's principle and then extend it

to single crystals and then polycrystalline grains in turn. Thus, the aforementioned averaging approach based on single domain properties can be used to predict polycrystalline ones using the tensor approach.

We have developed a new FE model based on the permeability tensors incorporating both microstructure and crystallographic texture and hence enabling a more accurate and robust prediction of the anisotropic behaviours of effective permeability. Moreover, our model considers the crystallographic orientation of each individual grain, as opposed to statistics, i.e., orientation distribution function (ODF) as usually seen in the literature e.g., [8], and hence is capable of capturing any local anisotropy (the effects of grain boundary misorientation on the electromagnetic interactions between adjacent grains and/or spatial distribution of the specific crystal orientations) as well as global anisotropy (the effects of texture on the effective permeability anisotropy for the microstructure as a whole).

2. Model

2.1. Formulation of permeability tensors

Assume a cubic crystal is composed of a large number (N) and equal size of elementary magnetic domains that can only orientate along one of the magnetic easy directions, i.e., cubic edges or the $\langle 100 \rangle$ directions. The magnetic structure of the elementary domains orientated along direction 1 is illustrated in Fig. 1. When a magnetic field h is applied along the direction 1, the induction of a consequential elementary domain along the direction 1 will be $\boldsymbol{B} = \mu_0 \mu_c h \hat{\mathbf{e}}_\mathbf{1}$, where μ_0 is the permeability of free space; μ_c is the scale constant defined as relative elementary permeability, by analogy to the continuum counterpart, the relative permeability, for the elementary domain along direction 1; $\hat{\mathbf{e}}_\mathbf{1}$ is the unit vector for direction 1. When h is applied along the other orthogonal directions, i.e., the direction 3 and 5, the induction will be $\boldsymbol{B} = \mu_0 h \hat{\mathbf{e}}_\mathbf{3}$ and $\boldsymbol{B} = \mu_0 h \hat{\mathbf{e}}_\mathbf{5}$ respectively. In other words, the direction 1, 3 and 5 are three principal directions along which relative elementary permeability values are μ_c, 1 and 1 respectively. Therefore, the relative elementary permeability tensor for direction 1 can be represented by

$$\boldsymbol{\mu}_1 = \begin{bmatrix} \mu_c & 0 & 0 \\ 0 & 1 & 0 \\ 0 & 0 & 1 \end{bmatrix} \tag{1}$$

The relative elementary permeability tensors for the other easy directions can be easily obtained by symmetry and orientation rotation:

$$\boldsymbol{\mu}_2 = \boldsymbol{\mu}_1, \quad \boldsymbol{\mu}_3 = \boldsymbol{\mu}_4 = \begin{bmatrix} 1 & 0 & 0 \\ 0 & \mu_c & 0 \\ 0 & 0 & 1 \end{bmatrix}, \quad \boldsymbol{\mu}_5 = \boldsymbol{\mu}_6 = \begin{bmatrix} 1 & 0 & 0 \\ 0 & 1 & 0 \\ 0 & 0 & \mu_c \end{bmatrix} \tag{2}$$

where the subscript denotes the six easy directions as shown in Fig. 1.

The following assumptions, after Bozorth [26], are applied:

(1) When the crystal as a whole is not magnetised, all the domains orientate along the six easy directions by equal probability.

(2) When an external magnetic field is applied, the crystal is magnetised by re-distributing the numbers of the domains across the six directions represented by $\mathbb{N} = \{N_1, N_2, \ldots, N_6\}$, which will be referred to as the domain configuration, favouring those closest to the external field direction.

(3) The resulting magnetisation must have a component along the given field direction.

Heisenberg originally made the first two assumptions in 1930s, which have since become widely accepted as part of domain theory. Mathematically, the most probable domain configuration for a single crystal has already been solved by Bozorth [26]:

$$\begin{aligned} N_1 &= e^{\alpha+\beta\gamma_x} \quad N_3 = e^{\alpha+\beta\gamma_y} \quad N_5 = e^{\alpha+\beta\gamma_z} \\ N_2 &= e^{\alpha-\beta\gamma_x} \quad N_4 = e^{\alpha-\beta\gamma_y} \quad N_6 = e^{\alpha-\beta\gamma_z} \end{aligned} \tag{3}$$

where α and β can be determined from the following equations

$$\frac{\gamma_x \sinh(\gamma_x\beta) + \gamma_y \sinh(\gamma_y\beta) + \gamma_z \sinh(\gamma_z\beta)}{\cosh(\gamma_x\beta) + \cosh(\gamma_y\beta) + \cosh(\gamma_z\beta)} = \frac{B_h}{B_s} \tag{4}$$

$$2e^{\alpha}(\cosh(\gamma_x\beta) + \cosh(\gamma_y\beta) + \cosh(\gamma_z\beta)) = N \tag{5}$$

$$N = N_1 + N_2 + N_3 + N_4 + N_5 + N_6 \tag{6}$$

where B_h is the component of the induction $\boldsymbol{B}$ along the applied field direction defined by the direction cosine $(\gamma_x, \gamma_y, \gamma_z)$ with respect to crystal direction 1, 3 and 5; B_s denotes the saturation induction. The effective permeability tensor for a single crystal with the domain configuration $\mathbb{N}$ can be obtained by tensor addition as follows

$$\boldsymbol{\mu}_{sc} = \frac{1}{N} \sum_{i=1}^{6} N_i \boldsymbol{\mu}_i \tag{7}$$

We now have formulated permeability tensors for an ideal single crystal in its own crystal reference frame. The relative permeability tensor for an arbitrary orientation with respect to the specimen reference frame, which is conventionally chosen to consist of the rolling direction (RD), transverse direction (TD) and normal direction (ND) as three axes, can be given as

$$\boldsymbol{\mu}_g = \mathbf{g}^{-1} \boldsymbol{\mu}_{sc} \mathbf{g} \tag{8}$$

where $\mathbf{g}$ is the crystal orientation represented by an orientation matrix (refer to [27] for the defintion of $\mathbf{g}$ and more details on relevant crystallography). Now consider a grain in a polycrystalline microstructure with orientation $\mathbf{g}$ and grain diameter d. The grain size effect needs considering. Assume the elementary domains on grain boundaries are not orientated along any easy directions, $\mathbb{N}$ will decrease proportionally with the volume fraction of the grain boundaries given by $6t/d$, where t denotes the grain boundary thickness. One can correlate t with the misorientation of the grain boundaries to consider the local anisotropy. The domain configuration in the present model, as a statistical representation of domain directions, does not consider the locality and morphology of the domains within a grain. The closure domains that are expected to be present near grain boundaries can be considered as two groups of elementary domains: one that parallels with any of the easy directions and the other that does not. The effects of the former are already taken into account as presumably less favoured easy directions; those of the latter are considered not to contribute to the permeability tensor. For simplicity in the present paper we consider the overall effects of the loss of the unparallel elementary domains by modifying each element in the domain configuration per unit volume in the polycrystalline grain as follows

$$N_i' = N_i(1 - \frac{c_g}{d}) \tag{9}$$

where c_g is a material parameter that can be measured experimentally. Note N_i' reduces to N_i when d approaches infinity, which is equivalent to a stand-alone single crystal. Combining Equations (7), (8) and (9) one obtains the permeability tensor for the grains in polycrystalline microstructures as a function of the crystallographic orientation, grain size and the domain configuration:

$$\boldsymbol{\mu_g'} = \mathbf{g^{-1}} \left[\frac{1}{N} \sum_{i=1}^{6} N_i (1 - \frac{c_g}{d}) \boldsymbol{\mu}_i \right] \mathbf{g} \tag{10}$$

2.2. Finite element microstructure model

A FE microstructure model based on the above permeability tensors was developed in MATLAB. The model considers a magnetostatics problem that involves a uniform static field applied to the microstructure. Substituting the constitutive equation

$$\boldsymbol{B} = \mu_0 \boldsymbol{\mu}_r \boldsymbol{H} \tag{11}$$

into the Maxwell's equations for magnetostatics and choosing the Columb gauge condition, $\nabla \cdot \boldsymbol{A} = 0$, one obtains the governing partial differential equation

$$-\nabla \cdot (\frac{1}{\mu_0 \boldsymbol{\mu}_r} \nabla \boldsymbol{A}) = J \tag{12}$$

where $\boldsymbol{A}$ is the vector potential, J the external current density, $\boldsymbol{\mu}_r$ denotes the relative permeability for the materials, which would be 1 for air and $\boldsymbol{\mu_g'}$ for the microstructure. To simulate uniform applied fields a Dirichlet boundary condition of uniform magnetic flux density, B_b, is applied to the model. The vector potential $\boldsymbol{A}$ can be broken down into two parts as

$$\boldsymbol{A} = \boldsymbol{A}_r + \boldsymbol{A}_b \tag{13}$$

where $\boldsymbol{A}_r$ is the reduced vector potential and $\boldsymbol{A}_b$ denotes the vector potential that satisfies

$$\boldsymbol{B}_b = \nabla \times \boldsymbol{A}_b \tag{14}$$

One solution of A_b can be given as

$$\boldsymbol{A}_b = \begin{bmatrix} -0.5yB_{bz} \\ 0.5xB_{bz} \\ yB_{bx} - xB_{by} \end{bmatrix} \tag{15}$$

where x and y are the coordinates; B_{bx}, B_{by} and B_{bz} are the three components of $\boldsymbol{B}_b$. No external current density is applied, i.e., $J = 0$.

The geometry of the model consists of the microstructure and a surrounding circular region of air as shown in Fig. 2. The diameter of the air region is set to five times the maximum dimension of the micrograph. The microstructure is composed of a number of entities representing the grains each drawn as a polygon rather than a single-entity micrograph or digital image. The model accepts either virtual microstructures together with simulated crystallographic texture data or measured Electron Backscatter Diffraction (EBSD) data. A boundary condition of

$$\boldsymbol{n} \times \boldsymbol{A} = \boldsymbol{n} \times \boldsymbol{A}_b \tag{16}$$

is applied to the outer edge of the air region, Γ, which is considered to be far away from the microstructure to simulate the external magnetic flux density, where $\boldsymbol{n}$ denotes the unit normal vector.

It is important to note that $\boldsymbol{\mu}'_g$ is not a constant tensor but dependent on the induction $\boldsymbol{B}$ and hence the FE solution, $\boldsymbol{A}$. It follows that the FE model is non-linear and hence tends to be complex and computationally costly to solve. For simplicity and computational efficiency, we recursively solve the average B across the whole microstructure, as opposed to at all nodes, at each iteration step, as illustrated in the flow chart, Figure 3. The *Patternsearch* algorithm in the MATLAB Global Optimization Toolbox, is used and the model usually converges to a very small residual ($< 0.0001B_s$), typically within 20 iterations. In each *Patternsearch* iteration, the permeability tensor for each grain, $\boldsymbol{\mu}'_g$, is calculated for the current guess on the B_h value, referred to as B_{hs}. Now that $\boldsymbol{\mu}'_g$ is known the FE model is linear. The model is solved using MATLAB's Partial Differential Equation (PDE) Toolbox. From the model solution the B_h value for the microstructure, B_{hm}, is then calculated. The cost function for the *Patternsearch* optimisation is $F(B_{hs}) = |B_{hm} - B_{hs}|$. Adjust B_{hs} according to the *Patternsearch* algorithm and repeat. The solution of the linear FE model at the end of the optimisation process is taken, at a first approximation, as the solution to the non-linear problem.

The weak form of the governing equation for the above linear FE model in a solvable form by the PDE Toolbox is

$$-\nabla \cdot (\boldsymbol{c}\nabla \boldsymbol{A}) + \boldsymbol{a}\boldsymbol{A} = \boldsymbol{f} \tag{17}$$

where the coefficients $\boldsymbol{c}$, $\boldsymbol{a}$ and $\boldsymbol{f}$ are specified as follows as per the rules set out in [28]. For the air domain, $\boldsymbol{c} = \frac{1}{\mu_0}$, $\boldsymbol{f} = \boldsymbol{A}_b$ and $\boldsymbol{a}$ is set to 1; for the whole microstructure $\boldsymbol{a}$ is set to 0 and $\boldsymbol{f}$ a 3×1 zero vector; for each individual grain,

$$\boldsymbol{c} = \begin{bmatrix} \nu_{11} & 0 & \nu_{12} & 0 & \nu_{13} & 0 \\ 0 & \nu_{11} & 0 & \nu_{12} & 0 & \nu_{13} \\ \nu_{21} & 0 & \nu_{22} & 0 & \nu_{23} & 0 \\ 0 & \nu_{21} & 0 & \nu_{22} & 0 & \nu_{23} \\ \nu_{31} & 0 & \nu_{32} & 0 & \nu_{33} & 0 \\ 0 & \nu_{31} & 0 & \nu_{32} & 0 & \nu_{33} \end{bmatrix} \tag{18}$$

where $\boldsymbol{\nu}$ is the inverse of $\boldsymbol{\mu}'_g$ for that grain and the subscripts denote the index of the element in $\boldsymbol{\nu}$.

The effective permeability of the microstructure, $\bar{\mu}$ can be evaluated from the FE solution by

$$\bar{\mu} \stackrel{\text{def}}{=} \frac{\|\boldsymbol{B}\|}{\mu_0 \|\boldsymbol{H}\|} \tag{19}$$

where $\|\boldsymbol{B}\|$ and $\|\boldsymbol{H}\|$ are the magnitude of $\boldsymbol{B}$ and $\boldsymbol{H}$ for the microstructure. The angle between the $\boldsymbol{B}$ and $\boldsymbol{H}$ vectors, Θ, is calculated by

$$\Theta = \arccos \frac{\boldsymbol{B} \cdot \boldsymbol{H}}{\|\boldsymbol{B}\| \|\boldsymbol{H}\|} \tag{20}$$

2.3. Microstructure and texture data

Virtual microstructures of targeted grain size and shape are simulated by the open-source software Neper [29]. To simulate texture data, ODFs were created given a mode of orientations and corresponding distribution kernel functions and half width for the spread, in the open-source MTEX toolbox for MATLAB [30]. In this paper, the default values, i.e., the de la Valee Poussin

function and 10° half width, were used; cubic crystal symmetry and orthorhombic specimen symmetry are also applied to all texture data. Crystal orientations were then generated from the ODFs and allocated randomly to each grain in the microstructure.

A separate MATLAB code was developed to convert the raster EBSD data into polygons with continuous and smoothed grain boundaries, as opposed to discontinuous segments available in commercial EBSD software packages, representing each grain ready for the FE geometry. The average grain orientations for each grain were calculated using the Aztec software package.

3. Modelling Results

3.1. Effects of crystallographic textures

To predict the separate effects of crystallographic texture on magnetic anisotropy, we allocated different textures to a virtual microstructure consisting of 500 grains whilst keeping the material parameters constant. μ_c is set to 1000, which, as a rule of thumb, will give predicted effective values of around 333 for random textures at a very small field (which has been measured experimentally for fully ferritic steel [31]). c_g is set to 0 to exclude the grain size effect. Fig. 4 shows the predicted effective permeability for some typical textures in steels including the fibre texture with $\langle 100 \rangle$ in parallel with ND, notated as $\langle 100 \rangle \parallel$ ND and also known as θ fibre, the γ fibre ($\langle 111 \rangle \parallel$ ND), the η fibre ($\langle 100 \rangle \parallel$ RD), the α fibre ($\langle 110 \rangle \parallel$ RD) and the Goss texture ($\{011\}\langle 100 \rangle$) along a series of directions swept from RD by 10° interval to 180°. All the curves are symmetrical with respect to the 90° axis as expected of the cubic crystal and specimen symmetry. The highest $\bar{\mu}$ values occur at RD for the η fibre and Goss texture which are both $\langle 100 \rangle$ directions, i.e., the magnetic easy direction; and the lowest value occurs at approximately 54.7° from RD for the Goss texture, which parallels with the $\langle 111 \rangle$, i.e., the magnetic hard directions. The γ fibre and the θ fibre exhibit isotropic permeability within the microstructure plane, which would be consistent with their in-plane random orientations, as a ND fibre, averaging out.

Fig. 5 shows the effective permeability maps for some selected textures and background field directions. The γ fibre (Fig. 5 (c)) and the Goss texture (Fig. 5 (i)) exhibit distinctive $\bar{\mu}$ maps despite very similar average $\bar{\mu}$ values (see Fig. 4). The former features more or less random $\bar{\mu}$ values across the microstructure indicating random in-plane orientations whilst the latter shows much less variation corresponding to the single texture (note the simulated uni-mode ODF for the single texture is not an ideal single crystal but has a 10° spread half width). Similarly, the

ND fibres, e.g., the γ fibre (Fig. 5(b)), exhibits more variation than the RD fibre, e.g., the α fibre (Fig. 5(d)), for the RD field direction. By comparison, the θ fibre map has systematically higher values than the γ fibre one and similar randomness across the microstructure. The Goss texture map features predominately uniform colors for each selected directions but are distinctive between each other.

The consistency in all these permeability behaviours demonstrates that the present model is capable of capturing the crystallographic texture effects on magnetic anisotropy. The predicted permeability curves serve as a quantitative characterisation of the magnetic anisotropy associated with texture. In addition, the permeability maps serve as an enhanced visual and quantitative indication of the textures as a supplement to inverse pole figure (IPF) maps.

Thanks to the tensorial permeability, as opposed to scalar ones, the model is also capable of predicting the angle between the $\boldsymbol{B}$ and the $\boldsymbol{H}$ vector, Θ. Fig. 6 shows the predicted average Θ values for the different textures. Similar to the effective permeability behaviours, the in-plane isotropy of the ND fibres including the γ and the θ fibres also manifests itself in the Θ behaviours. It is worth noting that Θ is without regard to the rotation axis direction. Thus, Θ values do not average out to be zero despite the in-plane isotropy as a whole. The Θ behaviours of the RD fibres and the Goss texture exhibit more undulated anisotropy than their effective permeability behaviours. The troughs appear to occur near the $\langle 100 \rangle$ direction, e.g. the RD for Goss and η fibre, the $\langle 110 \rangle$ direction, e.g., the RD for α fibre, as well as the $\langle 111 \rangle$ direction, e.g., 55° from RD for the Goss texture and the η fibre. This behaviour would be consistent with the literature [32, 33] reporting that these directions are the principal directions where $\boldsymbol{B} \parallel \boldsymbol{H}$.

3.2. Effects of uniform applied field strength

The uniform applied field magnitude, $\|\boldsymbol{B_b}\|$, normalised against B_s, is set to 0.1 for all the above modelling and the average $\|\boldsymbol{B}\|$ values of the microstructure, $\bar{B}$, eventually converge at 0.3–0.31. Owing to the non-linearity of the present model the predictions are also dependent on $\bar{B}$. Fig. 7 shows the $\bar{\mu}$ and Θ values as a function of $\bar{B}$ for the α fibre and the Goss texture for the $\boldsymbol{B_b}$ directions along which the maximum and the minimum $\bar{\mu}$ values occur respectively. The predicted $\bar{\mu}$ values for all the conditions increase from approximately 333, i.e. one third of the μ_c value, at different rates, by power laws as illustrated by the fitting lines. Similarly, the predicted Θ values also increase with $\bar{B}$ by power law. The order of both values for different conditions remain unaffected throughout the modelled range. The differences between the different $\boldsymbol{B_b}$ directions increase steadily indicating the anisotropy intensifies with the increase of

the normalised $\|\boldsymbol{B}\|$ field up to 0.4.

3.3. Effects of grain size

Fig. 8 shows the predicted $\bar{\mu}$ as a function of the average equivalent grain diameter, $\bar{d}$, for a series of virtual microstructures with different number of grains in a 1 mm×1 mm square and hence different $\bar{d}$, with and without considering the grain size effects. Random grain orientations were allocated to all the microstructures. The predicted $\bar{\mu}$ values increase with $\bar{d}$ fitting perfectly well with the power law by

$$\bar{\mu} = 362.2(1 - \frac{6.95}{\bar{d}}) \tag{21}$$

for $c_g = 6.95$ µm whilst remain constant at approximately 362.2 for $c_g = 0$. Note the remarkable similarity of Eq. (21) to Eq. (9). This behaviour also agrees well with the literature reporting the magnetic permeability values increase with the ferrite grain size by a similar inverse or inverse square root relationship in extra-low carbon steels [31, 34] or in non-orientated electrical steels [35]. The results prove that the present model has captured the grain size effects by considering the loss of elementary domains to the grain boundaries through introducing the parameter c_g. It is interesting and perhaps slightly counterintuitive at first view that the interactions of magnetic flux with the grain boundaries in the FE model, as manifested in the transition region near grain boundaries in the permeability maps as shown in Fig. 9, does not capture the grain size effect. Note where there is a decrease in the $\bar{\mu}$ values on one side of the grain boundaries, as compared to the bulk of the grain, there is increase on the other side cancelling it out. As a result, the effective $\bar{\mu}$ for the microstructure as a whole remains unchanged.

4. Measurements

4.1. Experimental details

A commercial grade GOES featuring strong texture was selected for experimental validation of the present model. EBSD data were collected across a large area of approximately 12×11 mm^2 at a step size of 10 µm. Fig. 10 shows the inverse pole figure maps exhibiting strong Goss texture and coarse grains as expected of this steel grade.

A small ($32 \times 15 \times 16$ mm^3) U-shaped electromagnetic (EM) sensor that can apply a relatively low magnetic field was used to measure an A4-sized thin (0.25 mm) GOES sheet at a series

of angles (φ) with respect to the RD. The relative permeability values were then indirectly extracted by non-linear least square regression. More details about the measurement system and the finite element modelling approached can be found elsewhere [36].

4.2. Identification of the model parameters

The grain size parameter c_g was set to 0 for simplicity considering the predominantly coarse grains and hence expectedly insignificant effects of c_g on the permeability values. The unknown material parameter μ_c were identified by *Patternsearch* optimisation algorithm fitting the predicted effective permeability values with the measured ones and at the same time recursively solving $\bar{B}$. Fig. 11 shows the optimised predictions of the permeability values as a function of φ agreeing reasonably well with the measurements.

The permeability behaviours are also generally consistent with the predictions using the generated Goss texture data and virtual microstructure described in Section 3.1. μ_c has been identified to be 1497 with $\bar{B}$, for example, for $\varphi = 54.7$, having converged at approximately 0.6 and the Θ at approximately 24.9°. Fig. 12 shows the predicted $\bar{\mu}$ maps for the identified model parameters and the background field along RD, TD, ND and 54.7° with respect to RD. These maps visualise the following main characteristics of the magnetic anisotropy associated with the Goss texture corresponding to the IPF maps shown in Fig. 10. First, the RD maps shows generally highest permeability values indicating the RD being close to $\langle 100 \rangle$ directions. Second, the TD and ND ones are similar indicating these directions are close to the same crystal direction. The map for 54.7° from RD shows predominantly low permeability value indicating it is close to $\langle 111 \rangle$ directions.

It should be noted that the prediction of Θ values and the effects of B on the effective permeability anisotropy cannot be fully validated using the present measurement technique, which only measure scalar permeability (hence $\boldsymbol{B} \parallel \boldsymbol{H}$) and is not capable of changing the applied field strength (which is determined by the sensor geometry). A sensor system that can measure multiple $\boldsymbol{B}$ and $\boldsymbol{H}$ components is needed and being developed. The present tensor permeability model is fully capable of modelling 3D microstructures and any direction in 3D space although only 2D microstructures have been modelled in this paper. The 2D microstructure in-plane directions are often of more interest and probably more accurate as far as the microstructural effects are concerned.

The present model is anticipated to be used to provide the permeability anisotropy for predicting sensor measurements for low field EM sensors used for monitoring steel quality during

processing (e.g., [37]) and / or for the interpreting the EM sensor signals to infer the texture of the steel. The model could also be used to predict anisotropic effective permeability values that can be input into other macroscopic FE electromagnetic models as the material property, say, the permeability of electrical steel components of an electric motor, to consider the steel's microstructure and texture. As a FE microstructural model the present model may potentially be coupled with other microstructural models, e.g., the microstructure-based crystal plasticity models, for multi-physics modelling.

5. Conclusion

A tensorial permeability finite element microstructure model that considers crystallographic textures based on magnetic domain theories has been developed for evaluation of magnetic anisotropy of polycrystalline steels. The model can predict consistent and logical effective permeability behaviours and the angle between B and H for some selected typical textures that are important and common in steel manufacturing. The model has proved capable of capturing the crystallographic texture, the grain size and the background field effects on the magnetic anisotropy of steels based on the magnetic domain theory. The predicted effective permeability curves as a function of the magnetic field directions and the permeability maps can serve as a quantitative characterisation of the magnetic anisotropy as well as an enhanced visual indication of the crystallographic texture from magnetic values. These capabilities have been initially validated against a commercial grain oriented electrical steels featuring strong Goss texture and magnetic anisotropy.

Acknowledgements

The authors would like to thank Dr Frenk van den Berg from Tata Steel Europe for the useful discussion about the work. This project has received funding from the Research Fund for Coal and Steel under grant agreement No. 847296.

References

[1] R.E. Newnham, *Magnetic Phenomena*, in *Properties of Materials : Anisotropy, Symmetry, Structure*, chap. 14, Oxford University Press, 2005, pp. 122–146.

[2] K. Honda, S. Kaya, and Y. Masuyama, *On the Magnetic Properties of Single Crystals of Iron*, Nature 117 (1926), pp. 753–754.

[3] H.J. Williams, *Magnetic Properties of Single Crystals of Silicon Iron*, Phys. Rev. 52 (1937), pp. 747–751.

[4] A. Reuss, *Berechnung der Fließgrenze von Mischkristallen auf Grund der Plastizitätsbedingung für Einkristalle*, ZAMM - Zeitschrift für Angew. Math. und Mech. 9 (1929), pp. 49–58.

[5] W. Voigt, *Lehrbuch der Kristallphysik*, Vieweg+Teubner Verlag, Wiesbaden, 1966.

[6] R. Hill, *The Elastic Behaviour of a Crystalline Aggregate*, Proc. Phys. Soc. Sect. A 65 (1952), pp. 349–354.

[7] M. Kamaya, *A procedure for estimating Young's modulus of textured polycrystalline materials*, Int. J. Solids Struct. 46 (2009), pp. 2642–2649.

[8] L. Daniel and R. Corcolle, *A Note on the Effective Magnetic Permeability of Polycrystals*, IEEE Trans. Magn. 43 (2007), pp. 3153–3158.

[9] L. Kestens and S. Jacobs, *Texture Control During the Manufacturing of Nonoriented Electrical Steels*, Texture, Stress. Microstruct. 2008 (2008), pp. 1–9.

[10] A. Bükki-Deme, I. Szabó, and C. Cserháti, *Effect of anisotropic microstructure on magnetic Barkhausen noise in cold rolled low carbon steel*, J. Magn. Magn. Mater. 322 (2010), pp. 1748–1751.

[11] L. Zhou, C. Davis, P. Kok, F. Van Den Berg, S. Labbé, A. Martinez-de Guerenu, D. Jorge-Badiola, and I. Gutierrez, *Magnetic NDT for Steel Microstructure Characterisation – Modelling the Effect of Ferrite Grain Size on Magnetic Properties*, in *19th World Conf. Non-Destructive Test. (WCNDT 2016)*, Vol. 21, Munich, Germany. NDT.net, 2016.

[12] L. Zhou, J. Shen, A. Martinez-De-Guerenu, D. Jorge-Badiola, I. Gutiérrez, P. Kok, F. van den Berg, S. Labbé, A. Skarlatos, C. Reboud, and P. Lombard, *Micro and macro microstructure modelling for the influence of grain size on magnetic properties in structural steel and modelled commercial sensor outputs*, in *12th ECNDT*, jun, Gothenberg. 2018, pp. ECNDT–0228–2018.

[13] W. Brix and K. Hempel, *Tensorial description of the rotational magnetization process in anisotropic silicon steel*, J. Magn. Magn. Mater. 41 (1984), pp. 279–281.

[14] M. Birkfeld, *Investigation of the permeability tensor of electrical steel sheet*, IEEE Trans. Magn. 34 (1998), pp. 3667–3673.

[15] R. Langman, *Prediction and measurement of rotation of magnetization in an anisotropic polycrystalline ferromagnetic material*, IEEE Trans. Magn. 17 (1981), pp. 1159–1168.

[16] M. Enokizono, S. Kanao, and K. Yuki, *Permeability tensor of grain-oriented silicon steel sheet*, J. Magn. Magn. Mater. 133 (1994), pp. 209–211.

[17] F. Martin, D. Singh, P. Rasilo, A. Belahcen, and A. Arkkio, *Model of Magnetic Anisotropy of Non-Oriented Steel Sheets for Finite-Element Method*, IEEE Trans. Magn. 52 (2016), pp. 1–4.

[18] J. Bastos and G. Quichaud, *3D modelling of a non-linear anisotropic lamination*, IEEE Trans. Magn. 21 (1985), pp. 2366–2369.

[19] G. Shirkoohi and J. Liu, *A finite element method for modelling of anisotropic grain-oriented steels*, IEEE Trans. Magn. 30 (1994), pp. 1078–1080.

[20] H. Pfutzner, *Rotational single sheet testers for multi-parametric testing of soft magnetic materials - A review*, in *11th IMEKO TC4 Symposium on Trends in Electrical Measurements and Instrumentation and 6th IMEKO TC4 Workshop on ADC Modelling and Testing 2001*. 2001, pp. 422–426.

[21] U. Aydin, F. Martin, P. Rasilo, A. Belahcen, A. Haavisto, D. Singh, L. Daniel, and A. Arkkio, *Rotational single sheet tester for multiaxial magneto-mechanical effects in steel sheets*, IEEE Trans. Magn. 55 (2019), pp. 1–10.

[22] M. Carpentieri, S. Vergura, V. Puliafito, and G. Finocchio, *Vector hysteresis model to describe micromagnetic structures*, in *2016 IEEE 2nd International Forum on Research and Technologies for Society and Industry Leveraging a better tomorrow (RTSI)*, sep. IEEE, 2016, pp. 1–4.

[23] P. Rasilo, D. Singh, U. Aydin, F. Martin, R. Kouhia, A. Belahcen, and A. Arkkio, *Modeling of Hysteresis Losses in Ferromagnetic Laminations Under Mechanical Stress*, IEEE Trans. Magn. 52 (2016), pp. 1–4.

[24] J.B. Padilha, P. Kuo-Peng, N. Sadowski, and N.J. Batistela, *Vector Hysteresis Model Associated to FEM in a Hysteresis Motor Modeling*, IEEE Trans. Magn. 53 (2017), pp. 1–4.

[25] J.F. Nye (ed.), *Physical properties of crystals : their representation by tensors and matrices*, Clarendon Press, Oxford, 1985.

[26] R.M. Bozorth, *The Theory of the Ferromagnetic Anisotropy of Single Crystals*, Phys. Rev. 42 (1932), pp. 882–892.

[27] H.J. Bunge, *Orientation of individual crystallites*, in *Texture Analysis in Materials Science*, H.J. Bunge, ed., chap. 2, Butterworth-Heinemann, 1982, pp. 3–41.

[28] Mathworks, *Setting Up Your PDE*, in *Partial Differential Equation Toolbox User's Guide*, r2020b ed., chap. 2, Mathworks, 2020, pp. 69–88.

[29] R. Quey, P. Dawson, and F. Barbe, *Large-scale 3D random polycrystals for the finite element method: Generation, meshing and remeshing*, Comput. Methods Appl. Mech. Eng. 200 (2011), pp. 1729–1745.

[30] F. Bachmann, R. Hielscher, and H. Schaeben, *Texture Analysis with MTEX – Free and Open Source Software Toolbox*, Solid State Phenom. 160 (2010), pp. 63–68.

[31] L. Zhou, C. Davis, and P. Kok, *Steel microstructure – magnetic permeability modelling: The effect of ferrite grain size and phase fraction*, J. Magn. Magn. Mater. 519 (2021), p. 167439.

[32] R.M. Bozorth, *Determination of Ferromagnetic Anisotropy in Single Crystals and in Polycrystalline Sheets*, Phys. Rev. 50 (1936), pp. 1076–1081.

[33] H. Vande Sande, F. Henrotte, K. Hameyer, and L. Froyen, *A hybrid method for determining the reluctivity tensor components of Goss textured ferromagnetic materials*, COMPEL - Int. J. Comput. Math. Electr. Electron. Eng. 23 (2004), pp. 579–589.

[34] J. Liu, J. Wilson, C.L. Davis, and A. Peyton, *Magnetic characterisation of grain size and precipitate distribution by major and minor BH loop measurements*, J. Magn. Magn. Mater. 481 (2019), pp. 55–67.

[35] M. Shiozaki and Y. Kurosaki, *The effects of grain size on the magnetic properties of nonoriented electrical steel sheets*, J. Mater. Eng. 11 (1989), pp. 37–43.

[36] M. Aghadavoudi-Jolfaei, J. Shen, A. Smith, L. Zhou, and C. Davis, *Non-destructive measurement of microstructure and tensile strength in varying thickness commercial DP steel strip using an em sensor*, J. Magn. Magn. Mater. 473 (2019), pp. 477–483.

[37] F. van den Berg, P. Kok, H. Yang, M. Aarnts, J.J. Vink, W. Beugeling, P. Meilland, T. Kebe, M. Stolzenberg, D. Krix, A. Peyton, W. Zhu, A. Martinez-De-Guerenu, I. Gutierrez, D. Jorge-Badiola, K. Gurruchaga, P. Lundin, A. Volker, M. Mota, J. Monster, H. Wirdelius, C. Mocci, G. Nastasi, V. Colla, C. Davis, L. Zhou, R. Schmidt, S. Labbé, C. Reboud, A. Skarlatos, T. Svaton, V. Leconte, and P. LOMBARD, *In-line characterisation of microstructure and mechanical properties in the manufacturing of steel strip for the purpose of product uniformity control*, in *19th World Conference on Non-Destructive Testing*, Jun., Munich, Germany. 2016.

List of Figures

1 Schematic of magnetic structure of α–iron showing the magnetic moment directions of each atom in a crystal cell in its crystal reference frame represented by [100], [010] and [001] directions. The six magnetic easy directions are marked as numbers. . . . 19

2 Geometry and meshing of finite element microstructure model for a 1 mm×1 mm virtual microstructure consisting of 500 grains. The mesh is generated by MATLAB Partial Differential Equation Toolbox. . . . 20

3 A flow chart illstrating the recursive approach for solving the non-linear FE model. ξ denotes the tolerance for the Patternsearch algorithm. . . . 21

4 Predicted effective permeability for some important textures using a same virtual microstructure as a function of the directions of the applied field with respect to the RD. . . . 22

5 Predicted effective permeability maps for selected textures and field directions. The colors are mapped to the permeability values using a same virtual microstructure. (a) θ fibre along TD, (b) γ fibre along RD and (c) TD, (d) α fibre along RD, (e) η fibre along RD and (f) TD, and Goss texture along (g) RD, (h) 55° from RD and (i) TD. . . . 23

6 The average angle between the $\boldsymbol{B}$ and $\boldsymbol{H}$ of the virtual microstructure for some typical textures in steels. . . . 24

7 The effective permeability $\bar{\mu}$ (a) and the angle between $\boldsymbol{B}$ and $\boldsymbol{H}$ (b) as a function of $\bar{B}$ for the α–fibre texture with the $\boldsymbol{B}_b$ along RD and 45° from RD and for the Goss texture with $\boldsymbol{B}_b$ along RD and 54.7° from RD with a virtual microstructure consisting of 500 grains. The dashed lines are power law fitting. . . . 25

8 Predicted effective permeability as a function of the average grain size for a series of virtual microstructures. . . . 26

9 Predicted effective permeability maps for a series of virtual microstructure consisting of different number of grains, n_{gs} = (a) 100, (b) 200, (c) 500, (d) 1000, (e) 1500, (f) 2000. . . . 27

10 Inverse pole figure maps of the grain oriented electrical steel sample for the (a) rolling direction (RD) (b) transverse direction (TD) and (c) normal direction (ND) pole. . . . 28

11 Predicted permeability as a function of the field direction using the identified model parameters compared with the measured ones for the grain oriented electrical steel. . . . 29

12 Predicted permeability maps for the grain orientated electrical steel sample for different background field directions. (a) RD, (b) TD, (c) ND, (d) 54.7° from RD. 30

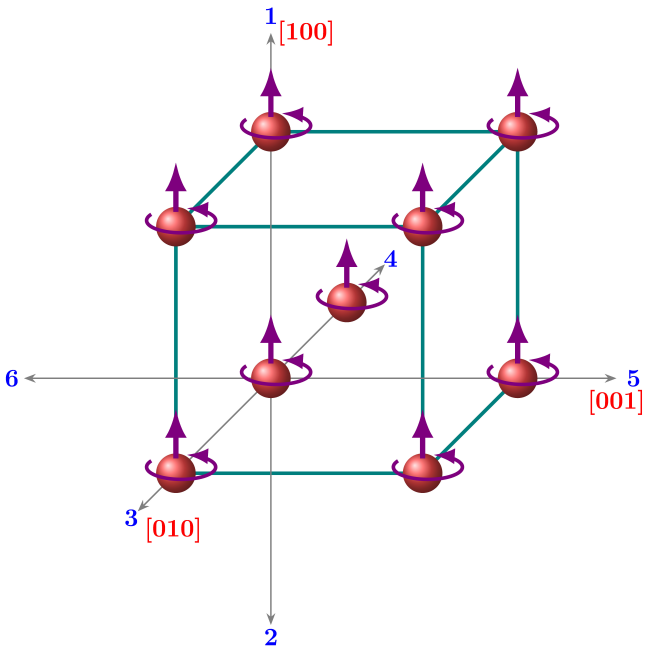

;

Figure 1. Schematic of magnetic structure of α–iron showing the magnetic moment directions of each atom in a crystal cell in its crystal reference frame represented by [100], [010] and [001] directions. The six magnetic easy directions are marked as numbers.

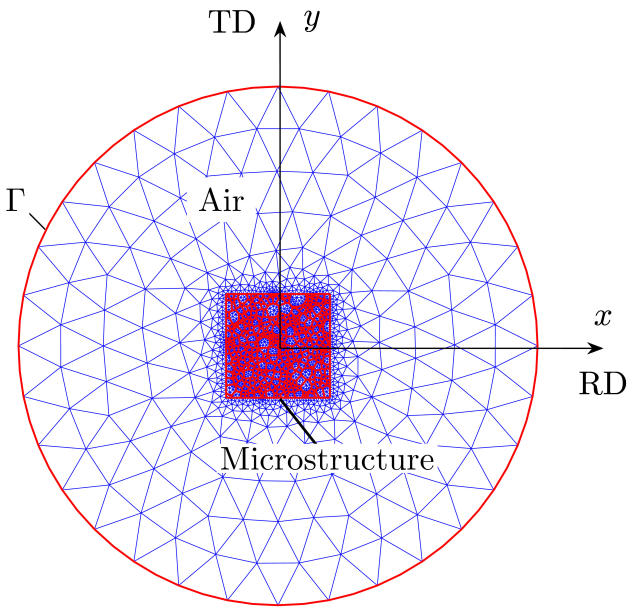

Figure 2. Geometry and meshing of finite element microstructure model for a 1 mm×1 mm virtual microstructure consisting of 500 grains. The mesh is generated by MATLAB Partial Differential Equation Toolbox.

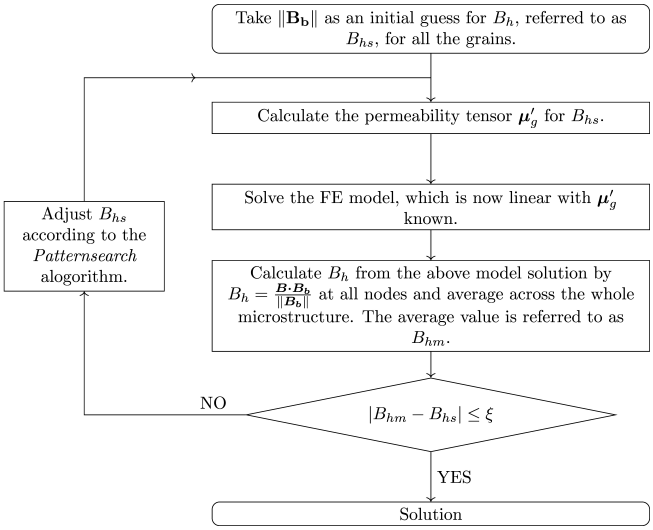

Figure 3. A flow chart illstrating the recursive approach for solving the non-linear FE model. ξ denotes the tolerance for the Patternsearch algorithm.

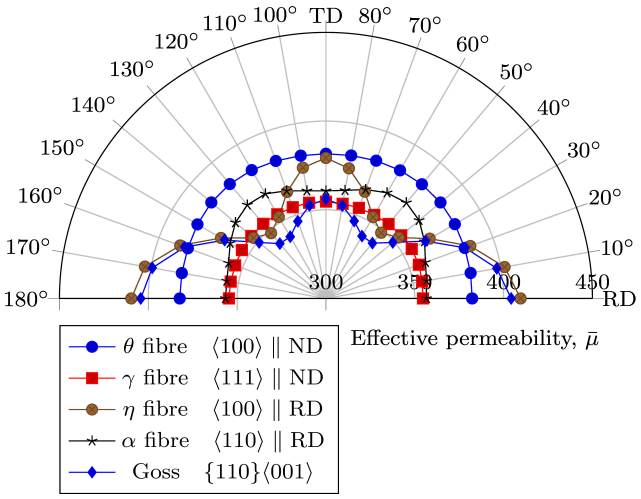

Figure 4. Predicted effective permeability for some important textures using a same virtual microstructure as a function of the directions of the applied field with respect to the RD.

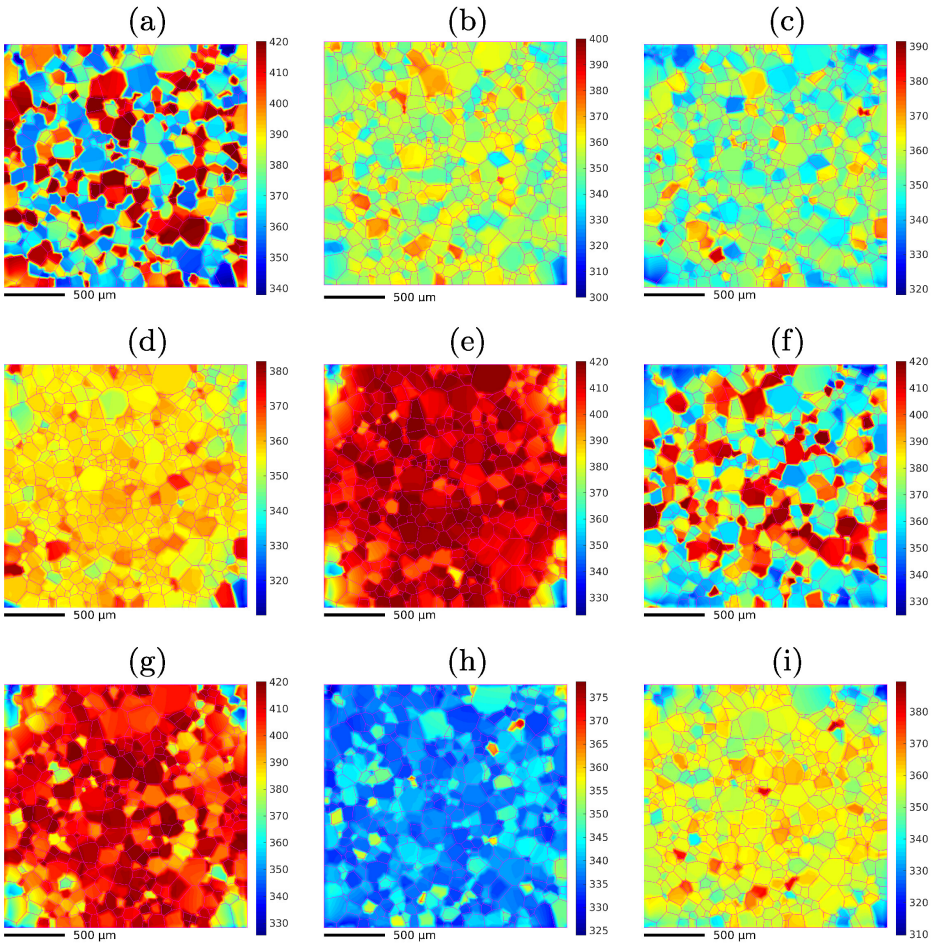

Figure 5. Predicted effective permeability maps for selected textures and field directions. The colors are mapped to the permeability values using a same virtual microstructure. (a) θ fibre along TD, (b) γ fibre along RD and (c) TD, (d) α fibre along RD, (e) η fibre along RD and (f) TD, and Goss texture along (g) RD, (h) 55° from RD and (i) TD.

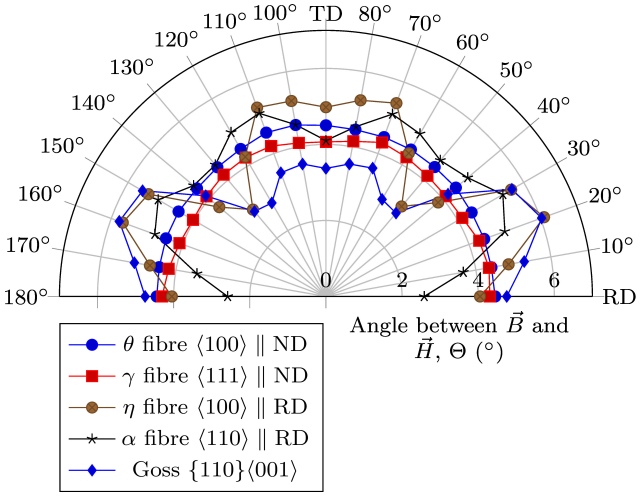

Figure 6. The average angle between the $\boldsymbol{B}$ and $\boldsymbol{H}$ of the virtual microstructure for some typical textures in steels.

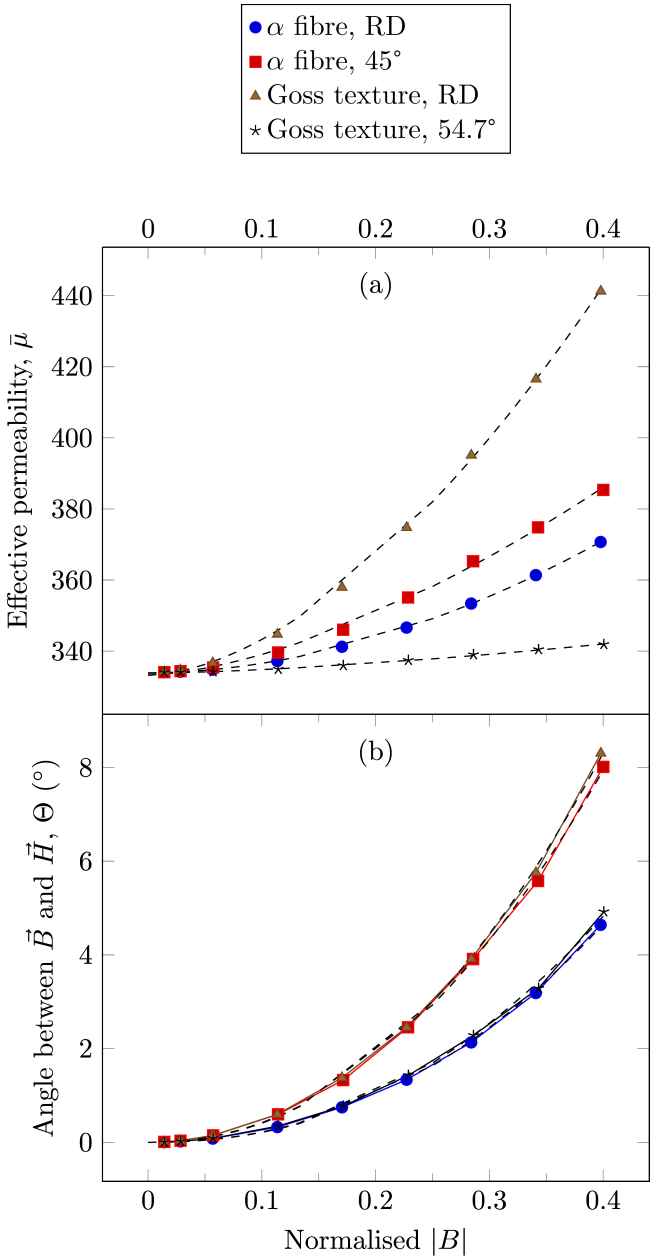

Figure 7. The effective permeability $\bar{\mu}$ (a) and the angle between $\boldsymbol{B}$ and $\boldsymbol{H}$ (b) as a function of $\bar{B}$ for the α–fibre texture with the $\boldsymbol{B}_b$ along RD and 45° from RD and for the Goss texture with $\boldsymbol{B}_b$ along RD and 54.7° from RD with a virtual microstructure consisting of 500 grains. The dashed lines are power law fitting.

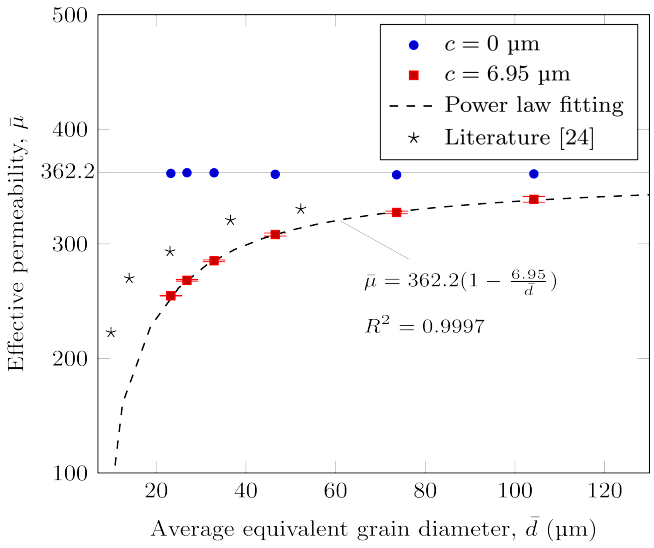

Figure 8. Predicted effective permeability as a function of the average grain size for a series of virtual microstructures.

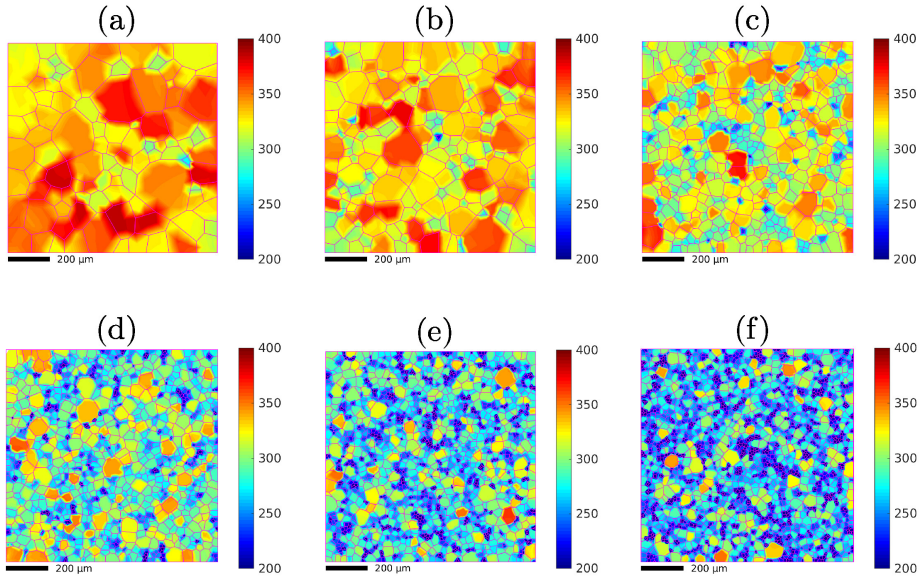

Figure 9. Predicted effective permeability maps for a series of virtual microstructure consisting of different number of grains, n_{gs} = (a) 100, (b) 200, (c) 500, (d) 1000, (e) 1500, (f) 2000.

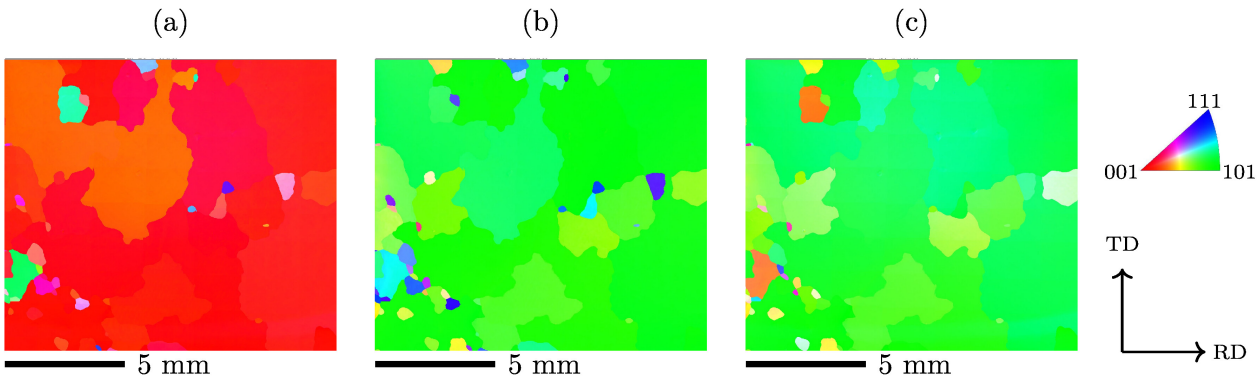

Figure 10. Inverse pole figure maps of the grain oriented electrical steel sample for the (a) rolling direction (RD) (b) transverse direction (TD) and (c) normal direction (ND) pole.

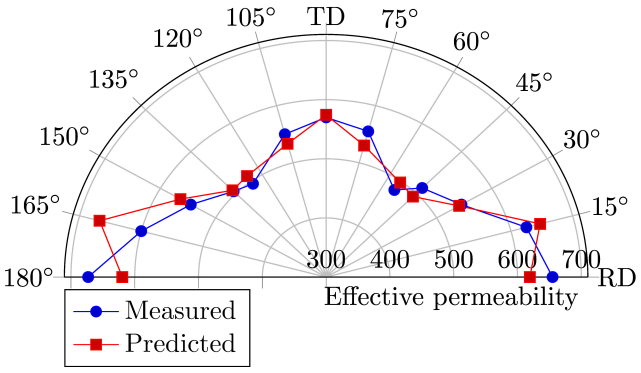

Figure 11. Predicted permeability as a function of the field direction using the identified model parameters compared with the measured ones for the grain oriented electrical steel.

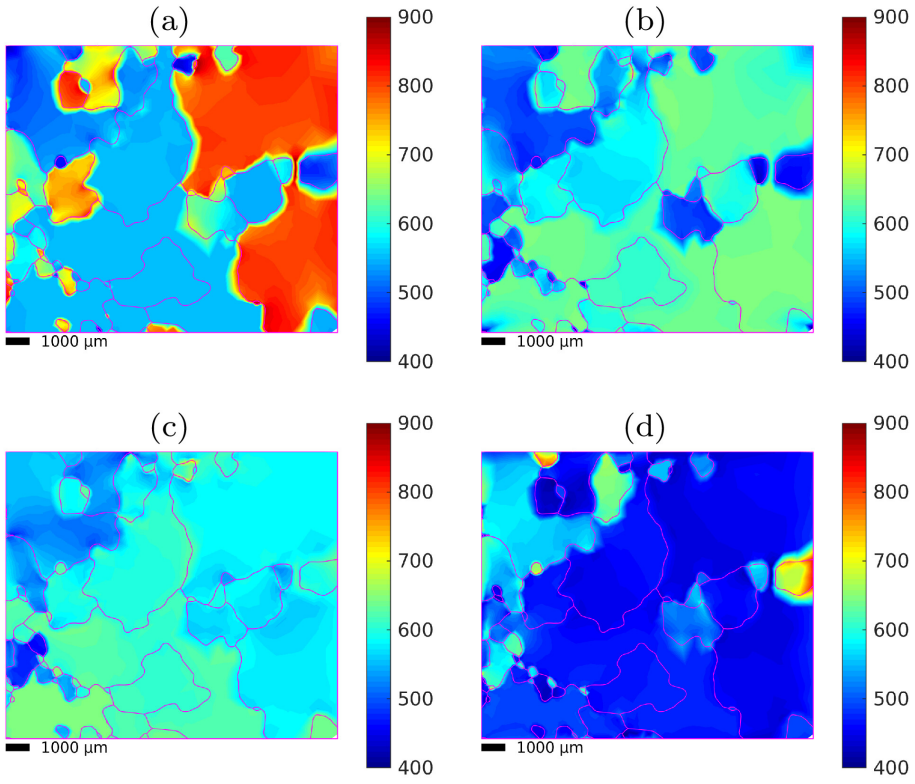

Figure 12. Predicted permeability maps for the grain orientated electrical steel sample for different background field directions. (a) RD, (b) TD, (c) ND, (d) 54.7° from RD.